A Non-Contact PCB Multi-Fault Diagnosis Algorithm Based on Scalar Magnetic Field Fusion Feature and Transformer Architecture

Chengxin Liu, Haiwen Yuan, Michele Ferlauto, Jianxun Lv, *Member*, *IEEE*, Yingyi Liu, and Hai Xu

***Abstract*—Non-contact printed circuit board (PCB) fault diagnosis has been widely applied in PCB detection and maintenance. Due to objective factors such as visual blind spots, low-loss circuit structure design, and frequency insensitivity, traditional algorithms based on visual and temperature features are limited in practice. Therefore, the algorithm based on electromagnetic features containing rich physical connotations and prominent frequency features has received attention in PCB fault diagnosis. Based on the basic principles of electromagnetic physics and PCB fault relationship, this article proposes a scalar magnetic field source feature and further improves feature performance by adding topological relationships of multi-faults to generate the fusion feature. The backbone of the PCB diagnosis model is established on the Transformer architecture, effectively utilizing self-attention and parallel computing mechanisms to explore the inner correlation between each group feature. The paper provides a new non-contact PCB fault diagnosis solution that enriches existing methods. Besides, through actual experiments setting up multi-fault PCBs, the feasibility of our process is proved based on the proposed features and models. The specific multiple indicators Overall Precision (OP), Per Class Precision (CP), Overall Recall (OR), Per Class Recall (CR), Overall F1 Measure (OF1), Per Class F1 Measure (CF1), Accuracy (ACC), Mean Average Precision (mAP) are 98.55%, 94.89%, 98.55%, 95.11%, 98.55%, 95.32%, 96.01%, and 97.27%.**

***Index Terms*—Non-contact, PCB, multi-fault, scalar magnetic field, fusion feature, Transformer.**

I. Introduction

With the rapid development of electronic information technology, the printed circuit board (PCB) with various functions used in advanced fields, such as energy transmission, mobile communications, and high-speed signal processing, has already had an enormous market demand [1], [2]. Correspondingly, the large-scale use of PCB also brings many faults in diagnosis and maintenance needs [3]-[5]. Modern PCBs usually involve multiple functional modules and high-frequency components, which may have complex electromagnetic characteristics and are susceptible to distributed parameter interference [6]. Therefore, an efficient and accurate rapid fault diagnosis algorithm for PCBs must be developed urgently.

Based on the PCB properties and the need for accurate diagnosis, non-contact fault diagnosis methods have colossal development potential [7]-[9]. The mature non-contact detection methods are mainly based on vision and temperature field features, which have achieved good results in some diagnostic issues targeting PCBs [10]-[12]. L. Lei et al., based on the visual method, used multi-scale convolution to extract and classify various faults in PCB visual images, and the experimental results showed high accuracy [13]. J. Zhu et al. used image segmentation and morphological methods to extract PCB defect features and got excellent diagnosis results [14]. However, it can be found that the visual methods lack a correlation between data and the physical characteristics of the PCB, which will cause the algorithm to be fragile when the PCB fault occurs in the visual blind areas.

To establish the physical correlation between data and detection targets, S. Y. Huang et al. proposed a coding method based on thermal imaging and compared all fault codes with no-fault PCB codes to achieve the recognition of abnormal functional blocks in PCBs [15]. W. He et al. established a PCB fault recognition system using the GAN network based on the feature set composed of wavelet cross-spectrum and wavelet coherence of infrared temperature data [16]. They effectively identified device performance anomalies. The current complex PCB structures and future development trends fully consider the damage caused by high temperature and energy consumption to the PCBs [17]-[19]. However, the temperature field needs to be established because the PCB has sufficient heat generation and temperature emissivity, which limits the

This research was supported by the National Natural Science Foundation of China (62473024 and 62073013) and the 5720 Factory and Beihang Science and Technology Cooperation Project and China Scholarship Council and the Fundamental Research Funds for the Central Universities. (*Corresponding author: Jianxun Lv, Yingyi Liu, Haiwen Yuan, and Michele Ferlauto*).

C. Liu is with the School of Automation Science and Electrical Engineering, Beihang University, and Department of Mechanical and Aerospace Engineering, Politecnico di Torino, Beijing 100191 and Turin 10129, China and Italy (e-mail: by2103028@buaa.edu.cn).

H. Yuan is with the School of Automation Science and Electrical Engineering, Beihang University, Beijing 100191, China (e-mail: yhw@buaa.edu.cn).

M. Ferlauto is with Department of Mechanical and Aerospace Engineering, Politecnico di Torino, Turin 10129, Italy (e-mail: michele.ferlauto@polito.it).

J. Lv, Y. Liu are with the School of Automation Science and Electrical Engineering, Beihang University, Beijing 100191, China (e-mail: lvjianxun@buaa.edu.cn; liuyingyi@buaa.edu.cn).

H. Xu is with the Wuhu Machinery Factory, Wuhu 241000, China (e-mail: Xuh1981@126.com).

Color versions of one or more of the figures in this article are available online at http://ieeexplore.ieee.org

applicability of temperature fields. Moreover, whether it is visual or temperature field data, they do not have the characteristic of significantly changing the frequency of PCB signals, making them unsuitable for handling PCB faults with complex frequency characteristics.

Compared to the traditional data features, electromagnetic field features come from PCB's inherent characteristics. It is a distributed representation of signal voltage and current in the circuit, constantly radiated along with the signal transmission in PCB [20], [21]. In addition, electromagnetic fields contain rich frequency characteristics of PCB signals, making them very suitable for handling PCB faults with complex frequency characteristics. R. G. Wright achieved qualitative judgment of PCB faults containing frequency characteristics by directly comparing the electromagnetic data collected by non-contact electromagnetic probes and spectrum analyzers, both in the presence and absence of PCB faults [22]. H. Huang et al. used statistical methods to identify the state of integrated circuits based on near-field electromagnetic field data [23]. Both types of research have effectively achieved fault detection of PCBs based on non-contact electromagnetic measurement schemes, but both lack objective judgment standards and rely on engineering experience. Z. Yao et al. used an improved momentum adaptive rate neural network algorithm based on multi-layer wavelet decomposition and magnetic image wavelet energy characteristics to complete PCB fault diagnosis based on the magnetic field [24]. H. F. Spence proposed a feature based on magnetic field two-dimensional FFT and further combined it with artificial neural networks to construct a non-contact PCB diagnosis method based on changes in near magnetic field [25]. Using traditional neural networks, this fault diagnosis makes the model construction process more flexible and diverse, improving the model's ability to handle complex PCB fault features. However, due to the network's small depth and simple structure and the risk of overfitting, its ability to handle complex multi-fault PCB problems is relatively limited [26], [27]. It is not difficult to find that most electromagnetic measurement instruments can often scan frequencies but can only obtain scalar electromagnetic field data. Meantime, the theory and methods for diagnosing problems with multiple faults simultaneously in PCBs are weak and scarce. Therefore, there is still significant development space for non-contact PCB fault diagnosis algorithms based on electromagnetic field data.

This article aims to establish an algorithm with substantial practical engineering value that can fully characterize the characteristics of PCB using scalar magnetic field data and accurately diagnose PCB faults. We have established a scalar magnetic field source feature, which utilizes the radiation magnetic field of a PCB to transform it into a derived scalar wave equation and obtain the characteristic values of the equivalent PCB source at the spatial measurement points. In the meantime, the local binary pattern (LBP) algorithm highlights and strengthens the behavior and patterns of magnetic field sources on spatial measurement points. Further, the paper applies graph neural networks (GNN) to generate auxiliary features based on the fault relationship to improve feature performance, and the Transformer framework is used to construct the fault diagnosis model. We fully utilize and combine the physical connotation of magnetic fields, topological characteristics of faults, self-attention mechanisms, and the advantages of parallel computing to explore a method for diagnosing the PCB with multiple faults. The algorithm is a new attempt at PCB fault diagnosis, comprehensively diagnosing circuit on/off faults, matching faults, performance degradation faults, and various combined faults. This paper provides detailed information on the inherent characteristics and applicability of traditional contact, non-contact visual, non-contact temperature, and non-contact electromagnetic field measurements for readers to further understand in the appendix.

II. The Principle of Scalar Magnetic Field Fusion Feature

To establish a feature representation method with strong PCB state representation capabilities, it is necessary to fully consider the physical and mathematical connections between features and the PCB. Based on the relationship between the scalar field and fault types, we convert the original data into space and frequency to establish a source main feature and a multi-fault topological relationship auxiliary feature.

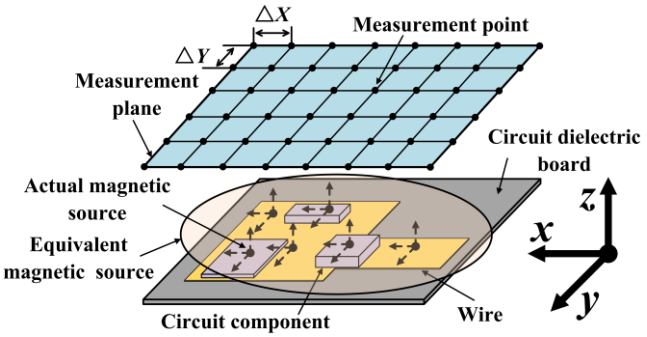

Fig. 1. Schematic diagram of non-contact magnetic field measurement for PCB

A. Principle of the scalar source feature

As a distributed representation of voltage and current, the electromagnetic field contains rich PCB operation information. In order to achieve accurate characterization of the working state of PCBs and overcome the objective reality that most measuring instruments are unable to capture complete magnetic field vector data $\vec{H}(\vec{r})$, we need to use the readily available scalar magnetic field data H_s to establish the electromagnetic characteristics of PCBs (This article uses magnetic fields as the primary data for research because electric and magnetic fields have duality, so the research method is similar. The duality principle is similar to the symmetry in Maxwell's equations, where electric and magnetic fields can be interchanged under certain conditions [28]).

In Fig. 1, the measurement plane consists of $m \times n$ magnetic field measurement points with a distance of ΔX and ΔY between the x-axis and y-axis. The PCB is composed of devices, wires, and media. PCB can be considered an equivalent magnetic field source composed of countless actual magnetic

field sources. This article presents a scalar equivalent magnetic source based on the basic Maxwell equation system. The magnetic field $\vec{H}(\vec{r})$ and electric field $\vec{E}(\vec{r})$ equations represented by the active Maxwell equation system are as follows:

$$\begin{cases} \nabla \times \vec{H}(\vec{r}) = j\omega\varepsilon_0 \vec{E}(\vec{r}) + \vec{J}(\vec{r_0}) \\ \nabla \times \vec{E}(\vec{r}) = -j\omega\mu_0 \vec{H}(\vec{r}) \end{cases} \tag{1}$$

where $\vec{r}$ is the magnetic field coordinate, $\vec{r_0}$ is the current source coordinate, ε_0 is the dielectric constant, μ_0 is the magnetic permeability, $\omega = 2\pi f$, f is the frequency, and $\vec{J}(\vec{r_0})$ is the current source. The following formula can be obtained by calculating the curl of Eq. (1) and converting it using vector identity:

$$\begin{aligned} \nabla\left(\nabla \cdot \vec{H}(\vec{r})\right) - \nabla^2 \vec{H}(\vec{r}) &= \nabla \times \left(\nabla \times \vec{H}(\vec{r})\right) \\ &= \nabla \times \left(\vec{J}(\vec{r_0}) + j\omega\varepsilon_0 \vec{E}(\vec{r})\right) \\ &= \nabla \times \vec{J}(\vec{r_0}) + j\omega\varepsilon_0 \left(\nabla \times \vec{E}(\vec{r})\right) \end{aligned} \tag{2}$$

Because the magnetic field is a divergence-free field and the electric field is a curl-free field, $\nabla \cdot \vec{H}(\vec{r}) = 0$ and $\nabla \times \vec{E}(\vec{r}) = 0$. The vector form of the active magnetic field wave equation can be organized as follows:

$$\nabla^2 \vec{H}(\vec{r}) + k^2 \vec{H}(\vec{r}) = \nabla \times \vec{J}(\vec{r_0}) \tag{3}$$

Since the result of calculating the curl of a vector current source is still a vector which can be set as $\nabla \times \vec{J}(\vec{r_0}) = \vec{C}(\vec{r_0})$ and Eq. (3) can be replaced by the equivalent source vector $\vec{C}(\vec{r_0})$. The specific formula is as follows:

$$\nabla^2 \left|\vec{H}(\vec{r})\right| \cdot e^{j\varphi} + k^2 \left|\vec{H}(\vec{r})\right| \cdot e^{j\varphi} = \vec{C}(\vec{r_0}) \tag{4}$$

where $k^2 = \omega^2 \mu_0 \varepsilon_0$ is the square of the wavenumber, $\left|\vec{H}(\vec{r})\right|$ and $e^{j\varphi}$ are the amplitude and phase terms of $\vec{H}(\vec{r})$. Since the left and right ends of the equation must be equal if the equivalent source vector $\vec{C}(\vec{r_0})$ is also written in the form of amplitude multiplied by phase, then the phase of $\vec{C}(\vec{r_0})$ must be equal to the phase $e^{j\varphi}$ of $\vec{H}(\vec{r})$. This way, Eq. (4) can be converted into a form of multiplying the equivalent magnetic field scalar source C_s by $e^{j\varphi}$, with the specific formula as follows:

$$(\nabla^2 H_s + k^2 H_s) \cdot e^{j\varphi} = C_s \cdot e^{j\varphi} \tag{5}$$

where H_s is the abbreviated form of $\left|\vec{H}(\vec{r})\right|$. Finally, we can simultaneously eliminate the phase term $e^{j\varphi}$ of Eq. (5) and further obtain a scalar wave equation composed of a scalar magnetic field H_s and an equivalent magnetic field scalar source C_s, as shown below:

$$\nabla^2 H_s + k^2 H_s = C_s \tag{6}$$

where the second-order Laplace term $\nabla^2 H_s$ is expressed as follows:

$$\nabla^2 H_s = \frac{\partial^2 H_s}{\partial x^2} + \frac{\partial^2 H_s}{\partial y^2} \tag{7}$$

In Fig. 2, the equivalent scalar source C_s that describes the magnetic field behavior at the current coordinate and frequency can be directly obtained by using the measured scalar magnetic field H_s and the corresponding frequency f. The C_s is a feature that includes the trend and local variation characteristics of PCB operation, which is a physical and mathematical mapping of PCB behavior. It is worth noting that C_s is mainly affected by the quadratic Laplacian term at low frequencies, while the influence of the scalar magnetic field term with the wave number increases rapidly with increasing frequency. In other words, C_s integrates the effects of space and frequency in a manner consistent with the laws of nature through physical equations. In contrast, aside from its inherent physical meaning, H_s, in terms of its representation, is merely a mathematical data point in the space and frequency coordinates, lacking any systematic correlation with these variables.

In addition, from a physical perspective, C_s can be seen as the specific manifestation of H_s at the spatial/frequency scale, with the overall PCB as the macroscopic radiation source. It includes the rate of change of H_s on the measurement plane point and the propagation behavior of H_s. From a mathematical perspective, by establishing a magnetic field scalar wave equation, the relationship between C_s, H_s, f, and measurement coordinates is described. It specifically describes the curvature and amplitude-frequency characteristics of H_s at the measurement point and, more profoundly, reflects the local variation law of the data. These characteristics also make C_s richer in connotation and more interpretable than H_s. From a data application perspective, the C_s derived is not formulated as an inverse problem of reconstructing current distribution from the measured magnetic field [5]. Instead, it is treated as a forward problem where the C_s is solved based on the known boundary conditions formed by the measured H_s. Therefore, the process of calculating C_s avoids the ill-posed process of the classical inverse problem of reconstructing currents from magnetic fields, and avoids the challenges associated with boundary condition variations caused by changes in current distribution due to PCB faults. In summary, C_s not only effectively reveals the states characteristics of the PCB but also ensures data interpretability, accuracy, and robustness.

B. Principle of the scalar source feature enhancement

In order to extract the primary law of PCB's various states, this article proposes a representation method of ELBP features based on equivalent magnetic field sources. In Fig. 3(a), we evaluated Eq (6) to calculate the LBP values of $m \times n \times F$ of C_s on every measurement frequency in the spatial coordinate

system, form the equivalent source LBP features (ELBP) based on equivalent magnetic field sources. By comparing the C_{sc} calculated at each measurement point in the spatial spectrum with the C_{si} of its surrounding neighborhood, the local texture information encoding in binary form of the source is obtained, and this encoding is converted into decimal numbers and stored at the measurement points as the texture feature values of the C_{sc}. The calculation formula for the ELBP value is as follows:

$$ELBP(F_i) = \sum_{j=1}^{8} f\left[C_{sj}(F_i) - C_{sc}(F_i)\right] \cdot 2^j \quad (8)$$

where,

$$f(x) = \begin{cases} 1 & , \quad x \geq 0 \\ 0 & , \quad x < 0 \end{cases} \quad (9)$$

$C_{sc}(F_i)$ is the center $C_s(F_i)$ value of each LBP calculation at the measurement points, $C_{si}(F_i)$ is the $C_s(F_i)$ value around $C_{sc}(F_i)$, F_i is the measurement frequency, $i = 1,2,\cdots,N$, and $j = 1,2,\cdots,8$. The C_{si} of this article adopts eight neighborhood values rotated clockwise starting from the top left corner of the C_{sc}, with a radius of 1. The C_{sc} at the edge, the measurement point is filled with 0 to complete the neighborhood C_{si}.

In PCBs, specific components exhibit performance variations due to extended operation time and temperature fluctuations. For example, the temperature rise in a power amplifier chip after prolonged use can reduce power gain, which in turn causes an overall decrease in output power. As a result, some of the measured local intensity data may show significant value changes but without distinct trend changes. As long as these variations fall within the designed performance range of the circuit, they do not indicate a fault in the circuit. ELBP, as a local texture feature, focuses more on the relative intensity between data points rather than their absolute values. This property ensures that performance fluctuations within the normal operating range of a PCB will not cause noticeable disturbances due to the electromagnetic data values' overall intensity variations. Instead, ELBP is more sensitive to the abnormal local trend changes between data points, making it particularly suitable for systems like PCBs that exhibit regular dynamic balance. In addition, ELBP is used to normalize C_s values on different frequency channels, further reducing the influence of extreme values. These inherent characteristics of the ELBP effectively ensure the data's stability and robustness.

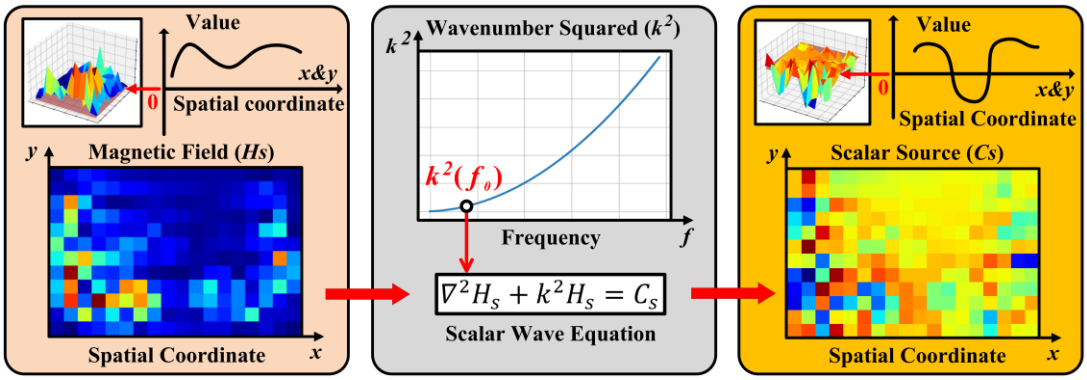

Fig. 2. Schematic diagram of converting the scalar magnetic field into the equivalent scalar source

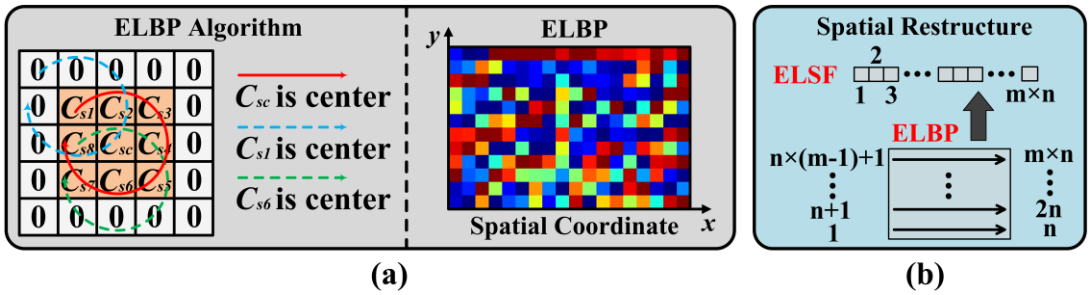

Fig. 3. Principle of ELSF algorithm based on LBP algorithm

In Fig. 3(b), this paper labels the m×n numbers of ELBP on the spatial coordinate system from one to m×n in order from left to right and from bottom to top, which forms the new spatial/frequency ELBP (ELSF) shown as follows:

$$ELSF = \{ELBP(F_1), ELBP(F_2), \cdots, ELBP(F_N)\} \quad (10)$$

The spatial transformation method turns the original four-dimensional structure into a three-dimensional structure, fixing the number of channels of the input data to 1, which is conducive to ensuring that the input of the model is not significantly affected by frequency and spatial point inconsistency and to the parallel operation of the subsequent model and further ensures the sharing of model parameters and reusing features between different levels.

C. Principle of the auxiliary features

To further enhance the diagnostic performance of the model, this article also introduces the auxiliary feature AF with PCB fault association. In Fig. 4, according to the faults to be

considered, we establish an undirected graph containing the connection relationship between them. The node represents each fault, and the connection line indicates whether there is a direct connection between the faults. The features of each node can be described by a binary number to store multi-fault features. Its length is the total number of faulty types, and the value in the binary position is that 1 represents such faults. This process can be understood as reflecting the objective structure of the PCB in the practical project and can be easily obtained from fault diagnosis problems. According to the graph's node vector and connection relationship, two layers of GNN are used to output a set of topological features AF that are the same as the ELSF dimension. The specific production AF is as follows:

$$AF = ReLU(D^{-0.5}AD^{-0.5}G_1W_2) \tag{11}$$

where,

$$G_1 = Dropout\big(ReLU(D^{-0.5}AD^{-0.5}G_0W_1)\big) \tag{12}$$

$$D_{ii} = \sum_j A_{ij} \tag{13}$$

$$Dropout(X) = R \cdot X = [R_1, \cdots, R_n] \cdot X \tag{14}$$

$$R_r = \begin{cases} 1 & , \quad p \\ 0 & , \quad 1-p \end{cases} \tag{15}$$

G_o is the node features, A is the adjacent matrix based on the faulty relationship, W_1 and W_2 are the weight matrix of the first and second layers of GNN, $ReLU(x) = \max(0, x)$, p is the retained probability for each neuron, $1-p$ is the dropped probability for each neuron, $r = 1, \cdots, n$.

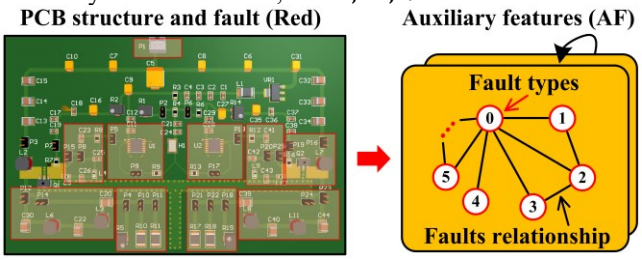

Fig. 4. Principle of auxiliary feature AF

III. The Principle of PCB Fault Diagnosis Model

In order to effectively apply ELSF and AF features, this paper establishes a Transformer training model with the self-attention mechanism. Based on this deep learning model, it establishes the mapping relationship between PCB fault features and PCB fault types, thereby rapidly detecting various faults on PCBs.

A. Input preprocessing

To make ELSF easier to understand and train by deep learning networks, we divide ELSF into N batches for parallel operations to improve the model efficiency. In Fig. 5, the ResNet has enhanced original features, giving ELSF more abstract, profound, and generalized feature representation capabilities. The network was constructed by using the following basic formula [29]:

$$\begin{cases} F = F_{IN} + Rn(F_{IN}, W_R) \\ Rn(F_{IN}, W_R) = W_R ReLU(W_{R-1}F_{IN}) \end{cases} \tag{16}$$

where F_{IN} and F are the inputs and outputs of the network, W_R is the weight of the R-th generation network.

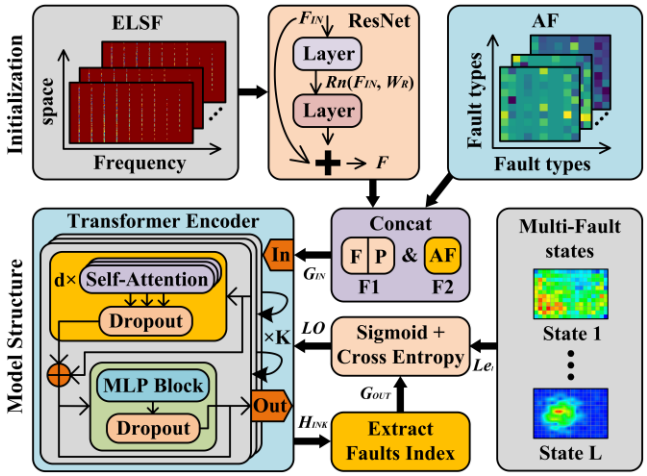

Fig. 5. The overall diagram of the PCB multi-fault diagnosis algorithm

In the Transformer model, the Self-Attention mechanism considers the interrelationships between various feature data when training the model, providing it with a powerful ability to capture global feature dependencies. However, this mechanism cannot directly distinguish the absolute positional information of different features. This article uses the two-dimensional position encoding method based on trigonometric functions to clarify the sequential relationship of input feature, which the specific equations as follows:

$$WD = exp\left(-\frac{2f}{D_{model}} \cdot log(10000)\right) \tag{17}$$

$$P_{PH\times PV} = \begin{cases} sin(posH \cdot WD) \\ cos(posH \cdot WD) \\ sin(posV \cdot WD) \\ cos(posV \cdot WD) \end{cases} \tag{18}$$

where $f = 1, \cdots, D_{model}/2$ is the index number of the frequency terms, D_{model} is the dimension of the ResNet output layer, PH and PV are the width and height of the ResNet output feature F. Finally, the Feature $F|P$ is the first feature F1, and the AF is the second feature $F2$, which stitches as the input feature of the Transformer. The formula formed is as follows:

$$G_{IN} = Concat[F1(F|P), F2(AF)] \tag{19}$$

B. Principle of model establishment

To enhance the model's learning ability and perceptual depth, we use d layer multi-head Attention mechanisms for K layer

stacking in the Transformer structure to parse and reinforce input features in parallel and serial. In the meantime, the Dropout mechanism is used to reduce overfitting and improve the robustness of the model. The operation process of the self-attention mechanism is as follows:

$$h_i = Attention(Q,K,V) = softmax\left(\frac{Q_i K_i^T}{\sqrt{Z}}\right)V_i \quad (20)$$

where,

$$Q_i, K_i, V_i = G_{IN}W_{Qi}, G_{IN}W_{Ki}, G_{IN}W_{Vi} \quad (21)$$

W_{Qi}, W_{Ki}, and W_{Vi} are the three weight matrices used to convert G_{IN} into Q_i (query), K_i (key), and V_i (value) matrices, Z is the scaling factor that ensures consistent gradients across different dimensional scales, $i = 1, \cdots, I$. Then, we can use the self-attention consisting of the multi-head to cooperate $Dropout$ mechanisms to generate multi-head outputs H_k as shown below:

$$\begin{aligned} H_k &= Dropout[MultiHead(Q_i, K_i, V_i)] \\ &= Dropout[Concat(h_1, \cdots, h_i, \cdots, h_I)W_C] \end{aligned} \quad (22)$$

where W_C is the weight matrix used to connect the multi-head module, h_i is the attention module of the i-th head, $k = 1, \cdots, K$.

Besides, the paper further improves the ability of the multi-head attention mechanism to pay more attention to the multi-scale information by using multi-layer perceptron (MLP) blocks and Dropout mechanisms between K Attention layers. These processes can effectively enhance the expressive power, stability, and attention to local and global information of the model. The output H_{INk_1} calculated by the MLP block and Dropout mechanism is as follows:

$$\begin{aligned} H_{INk_1} &= Dropout(MLP(H_k)W_P + b_1) \\ &= Dropout(ReLU(H_k + b_0)W_P + b_1) \end{aligned} \quad (23)$$

where W_P, b_0 and b_1 is the weight matrix and two bias vectors used to connect different layers. The label part in the output tensor of the Transformer Encoder will be separated in the Extract Faults Index module, and the probability value that can characterize the feature type will be obtained through scoring with the logits function and operation with the sigmoid function. The formulas for Logit function and Sigmoid function are as follows:

$$\begin{cases} Lg_l = Logit(G_{OUT}) = W_O \cdot G_{OUT} + b_2 \\ \widehat{Le}_l = sigmoid(L_l) = \frac{1}{1+e^{-Lg_l}} \end{cases} \quad l = 1, \cdots, L \quad (24)$$

where W_O and b_2 are the weight matrices and bias vectors of the Logit function, $\widehat{Le}_l$ is the probability value containing feature information.

In Fig. 6, we generate a string of all zero binary numbers which has the same number with the number of faults to be considered, and set the value corresponding to the fault index to 1, thereby forming an accurate label Le_l containing fault information. Because $\widehat{Le}_l$ is between 0 and 1 if the model output structure is the same as Le_l, the probability of $\widehat{Le}_l$ at the corresponding position of Le_l is the probability of the corresponding fault. The cross-entropy function can be used to calculate the loss value LO as the error feedback of the model, which specific equation is shown as follows:

$$LO = -\sum_{l=1}^{L}\left[Le_l \, log\, \widehat{Le}_l + (1 - Le_l)\, log\left(1 - \widehat{Le}_l\right)\right] \quad (25)$$

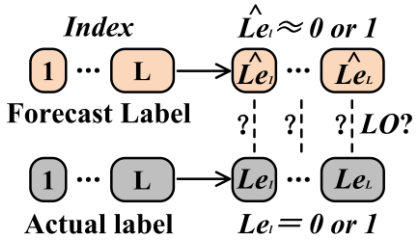

Fig. 6. Principle of PCB multi-fault label comparison

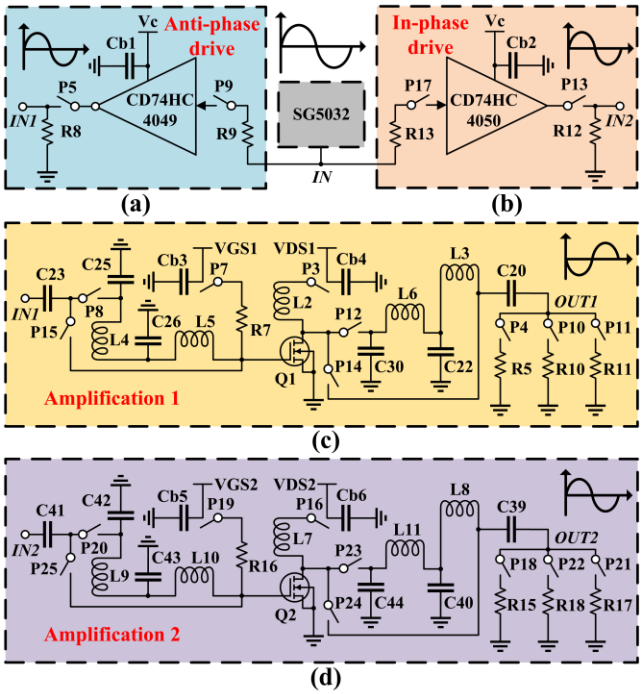

Fig. 7. Schematic diagram of the main functional modules of the DPPC

IV. Actual Experiments and Result Evaluation

In order to verify the effectiveness of the proposed PCB fault diagnosis algorithm, we designed and processed a fault-settable dual-phase amplifier circuit (DPPC) and used a magnetic field probe to collect its magnetic field amplitude data in various states for modeling. Finally, the effectiveness of the multi-fault diagnosis algorithm is verified by combining positive and negative problems, by setting PCB faults to obtain magnetic field data, and by determining PCB faults through magnetic field data.

A. Creation of actual objects

In Fig. 7, the DPPC designed in this article fully includes the phase reversal, phase maintenance, power amplification, DC power state, circuit matching, load status, and other typical problems to make the experimental object more typical.

In Fig. 7 (a) and 7 (b), we use the SG5032 crystal oscillator to provide input signal Vin, and add matching resistors $R9$, $R8$, $R17$, and $R12$ to the input and output ports of the dual-phase drive circuit composed of the CD74HC4049 antiphase chip and the CD74HC4050 in-phase chip, to ensure the output of phase voltage in both directions. In Fig. 7(c) and 7(d), to ensure power output, we designed two power amplification circuits with different parameters for the two circuits of the dual-phase drive circuit. In order to reduce losses and give full play to the power amplification capability of the N-type field effect transistor AFT05MS003N, we use multi-stage LC components at the input and output ports of the two circuits, which is a combination of methods to achieve circuit power matching.

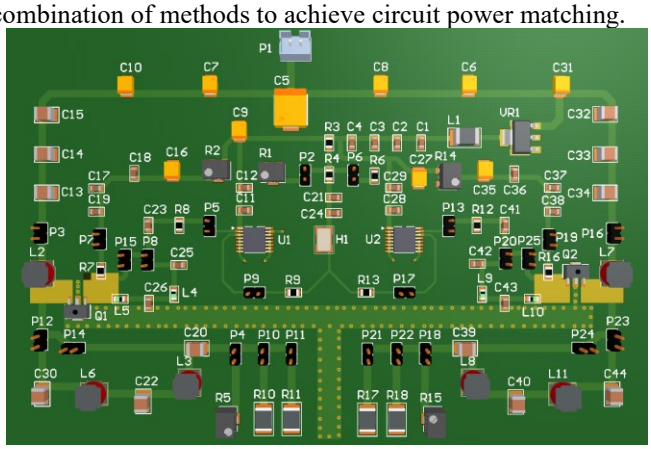

Fig. 8. The DPPC structure diagram

B. Experimental fault settings

Based on the above circuit functions, to verify the feasibility of the proposed algorithm for identifying faults in such complex functional circuits, we have added pluggable jumper blocks at some critical positions on the PCB to set typical faults for the PCB. It is worth noting that this article considers the on/off issues of the PCB signal path, power supply, and performance degradation caused by matching circuits, as well as load anomalies. In Fig. 8, we soldered the jumper block onto the back of the PCB and marked the jumper block number corresponding to the number on the front of the PCB to facilitate fault setting.

In Fig. 9, the paper provides a working voltage of 8 V to the DPPC through a digital adjustable DC power supply. It places the DPPC with several 5 mm diameter and 2 mm height silicone patches on the four top corners of the positive surface on the measurement plane of the EMxpert EHX electromagnetic scanner connected to the signal analyzer Kesight N9010B. The magnetic field radiation data of the DPPC is further collected through a personal computer. The EMxpert EHX scanner, the magnetic field acquisition device, comprises an array of 1218 (42×29) magnetic probes with 7.5 mm spacing, offering a spatial resolution of 3.75 mm. Paired with the N9010B, it enables the acquisition of magnetic fields over a spatial range of 316 mm × 218 mm and a frequency range of 150 kHz to 6 GHz in a single scan [30].

Table I shows the DPPC states set up in the experiment to verify the feasibility of the algorithm, as well as the jumper block numbers and corresponding operations involved in each state when a fault occurs separately (the setting of the state type here is not unique, the situation we set is to verify the feasibility of the algorithm, and other states can also be set according to this method for verification).

In order to verify the effectiveness of the algorithm in identifying multiple PCB fault states simultaneously, we combined all ten single states in Table I and considered a maximum of fourth-order situations where there are simultaneously four fault combinations. To ensure that the magnetic field data collected in this experiment is meaningful for algorithm validation, we conducted 10-20 random measurements on 128 individual and combined states in three scanning ranges at measurement heights of 6mm and 8mm, respectively, to further ensure the universality and diversity of magnetic field amplitude data. During this experiment, the scanning frequency range for each measurement was between 15MHz and 500MHz, with a scanning interval of 1MHz.

(a) (b)

Fig. 9. Actual testing platform

C. Experimental model details

In PCB electromagnetic measurement, the instrument may pick up background noise. In order to reduce the impact of such noise, we use the threshold filtering method on the original amplitude data, setting the magnetic field amplitude value below the threshold to 0. The paper sets the maximum value of PCB radiation magnetic field when not in operation as the threshold ε_{th}. The specific filtering formula is as follows:

$$H_{1D_f} = \begin{cases} H_{1D} & , \quad H_{1D} \geq \varepsilon_{th} \\ 0 & , \quad H_{1D} < \varepsilon_{th} \end{cases} \tag{26}$$

where H_{1D_f} is the filtered 1D magnetic field data that is used for the actual DSF calculation. The amount of data is set to Batch×Chennel×height×width= 8×1×500×500, which is used to complete the parallelization of the model and makes full use of the input data.

In the Transformer model, we use a multi-head mechanism consisting of self-attentions with a head count of $d = 8$ and a multi-layer structure with a stack count of $K = 4$ to enhance the depth and reliability of the Transformer structure. The Dropout mechanism used in the model randomly discards 10% of neurons to reduce overfitting probability and enhance the robustness of the network. The update of the overall model

weights is achieved using an Adam optimizer with second-order momentum [31], where the learning rate is $lr = 2 \times 10^{-5}$, the attenuation parameter is $[\beta_1, \beta_2] = [0.9, 0.999]$, and the stability constant is $\varepsilon = 10^{-8}$.

TABLE I
THE DPPC SINGLE FAULT STATE SETTING METHOD

The considered DPPC statuses	The involved jumper blocks
Reverse phase drive circuit fault	Cut P9 or Cut P5
Reverse phase drive circuit fault	Cut P17 or Cut P13
Input matching fault of PA1	Cut P8 & Connect (Con) P15
Output matching fault of PA1	Cut P12 & Con P14
Input matching fault of PA2	Cut P20 & Con P25
Output matching fault of PA2	Cut P23 & Con P24
Load fault of PA1	Cut P10 & (Con P4 or Con P11)
Load fault of PA2	Cut P22 & (Con P18 or Con P21)
DC power fault	Cut P1 or P3 or P7 or P16 or P19
Normal state	Not operate any jumper blocks

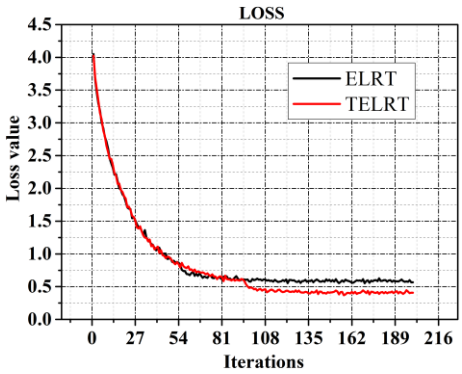

Fig. 10. The loss convergence process of ELRT and TELRT

D. Actual performance evaluation of the algorithm

This article uses an 8-to-2 ratio to divide the modeling samples randomly and uses them for the training and validation sets of the modeling, respectively. We use ResNet18 (This article does not use any pre-trained weights for any model) as the Transformer architecture input preprocessing network to train ELSF to form the Transformer fault diagnosis model based on ELSF (ELRT) and further incorporate topological features AF based on ELSF to form Transformer fault diagnosis model based on ELSF and AF bicharacteristic features (TELRT). Fig. 10 shows that the loss values of ELRT and TELRT gradually decrease and tend to stabilize, the training results converge, and the convergence process is stable.

In order to further verify the effectiveness and advantages of the ELRT and TELRT, we also compared and trained other classification features on the ResNet18 in the feature space/frequency coordinates established in this paper, explicitly involving scalar magnetic field features (MSF), equivalent magnetic field source features (ESF), magnetic field LBP features (MLSF), and ELSF. Meanwhile, we use multiple quantitative indicators to simultaneously measure the overall performance of each model, including Overall Precision (OP), Per Class Precision (CP), Overall Recall (OR), Per Class Recall (CR), Overall F1 Measure (OF1), Per Class F1 Measure (CF1), Accuracy (ACC), Mean Average Precision (mAP), and maximize the fairness of the evaluation of experiment results [32]. The calculation formula for each evaluation indicator is as follows:

$$\begin{aligned} OP &= \frac{\sum_{i=1}^{N} N_i^c}{\sum_{i=1}^{N} N_i^p} & CP &= \frac{1}{C}\sum_{i=1}^{N} \frac{N_i^c}{N_i^p} \\ OR &= \frac{\sum_{i=1}^{N} N_i^c}{\sum_{i=1}^{N} N_i^g} & CR &= \frac{1}{C}\sum_{i=1}^{N} \frac{N_i^c}{N_i^g} \\ OF1 &= \frac{2\times OP\times OR}{OP+OR} & CF1 &= \frac{2\times CP\times CR}{CP+CR} \\ ACC &= \frac{\sum_{i=1}^{N} N_i^c}{N} & mAP &= \frac{\sum_{i=1}^{N} AP_i}{N} \end{aligned} \tag{27}$$

where N_i^c is the number of correctly predicted i-th faults, N_i^p is the number of predicted i-th faults, W is the actual number of i-th faults, AP_i is the average accuracy of i-th faults, C is the number of faults to be predicted, and N is the total number of samples. Table II shows the comprehensive test results of MSFR, ESFR, MLSFR, and ELSFR under optimal weight by MSF, ESF, MLSF, and ELSF matching with ResNet18 and the results of ELRT and TELRT.

The experimental results show that our proposed feature and model significantly improved performance compared to the original field feature and the basic ResNet model. The specific results are as follows:

1) Compared to MSFR, ELSFR performs better in identifying overall and individual fault categories, with improvements of 1.22%, 2.52%, 6.83%, 1.87%, 2.95%, and 6.53% in OP, OR, CR, OF1, CF1, and ACC. However, in CP and mAP, ELSFR is smaller than MSFR by 1.38% and 0.24%. The results show that ESFR is more comprehensive and stable in identifying and capturing correct instances, especially in terms of significant improvement in accuracy.
2) Compared with MSFR and ESFR, the fault features enhanced by the LBP texture algorithm have more robust performance, especially ELSFR, which has stronger comprehensive performance, 0.02%, 5.08%, 0.94%, 1.83%, 0.49%, 3.38%, 1.57%, and 0.26% stronger than MLSFR in OP, CP, OR, CR, OF1, CF1, ACC, and MAP.

3) Compared with ELSFR, the overall performance of the ELRT model with the addition of the Transformer structure is better, mainly manifested in significant improvements of 2.46% and 2.18% in CR and ACC. At the same time, the TELRT formed by adding additional auxiliary features under the Transformer structure has further improved overall performance compared to ELRT, with specific improvements of OP, CP, OR, CR, OF1, CF1, ACC, and mAP in 0.01%, 3.20%, 0.63%, 5.49%, 0.32%, 4.68%, 1.33%, and 3.09%.

The results indicate that the Transformer framework can effectively improve the model's performance. Based on the physical laws of electromagnetic fields, ELSF has a more vital ability to characterize PCB states. Meanwhile, by simply adding AF, ELSF's ability to represent PCB states can be effectively improved, strengthening the performance of fault diagnosis algorithms.

In addition, in the PCB multi-fault diagnosis problem, the last "Normal state" mentioned in Table I should be noted. Because the Normal state is entirely independent of other faults and will not appear simultaneously as any other fault, it will inevitably lead to a smaller amount of data than other faults. We can see that the mAP of all algorithms in Table II is higher than that of ACC, which shows that they can still maintain a high balance and reliability of the algorithm when dealing with such sample imbalance problems. However, the overall performance degradation caused by small samples is inevitable. Here, we give the OP, CP, OR, CR, OF1, CF1, ACC, and MAP of TELRT when the normal state is not considered as 99.11%, 98.48%, 98.99%, 98.61%, 99.05%, 98.54%, 97.42%, and 99.88%. It can be seen that the quantitative indicators of the TELRT algorithm are high, and the overall indicators are balanced, which further verifies the excellent performance of TELRT. In order to realize the fault diagnosis of all states of PCB in practice, we must take the particular case of "Normal state" into account. Otherwise, the no-fault PCB will be misjudged. Therefore, we use the results in Table II as the primary research results of this paper.

TABLE II
COMPARATIVE EXPERIMENTAL RESULTS OF NEURAL NETWORK

Algorithm	OP	CP	OR	CR	OF1	CF1	ACC	mAP
MSFR	93.99%	84.45%	92.57%	76.07%	93.28%	80.04%	77.15%	89.04%
ESFR	95.21%	83.07%	95.09%	82.90%	95.15%	82.99%	83.68%	88.80%
MLSFR	98.32%	87.49%	96.10%	85.33%	97.20%	86.40%	90.93%	92.50%
ELSFR	98.34%	92.57%	97.04%	87.16%	97.69%	89.78%	92.50%	94.24%
ELRT	98.54%	91.69%	97.92%	89.62%	98.23%	90.64%	94.68%	94.18%
TELRT	98.55%	94.89%	98.55%	95.11%	98.55%	95.32%	96.01%	97.27%

TABLE III
COMPARATIVE EXPERIMENTAL RESULTS OF TRADITIONAL ALGORITHM

Algorithm	OP	CP	OR	CR	OF1	CF1	ACC	mAP
MSVM	99.57%	89.76%	88.04%	74.47%	93.45%	79.72%	77.39%	76.53%
MGNB	56.16%	54.77%	88.11%	89.16%	68.59%	65.32%	28.05%	51.27%
MRF	98.42%	89.97%	93.83%	84.06%	96.07%	86.72%	88.51%	83.33%
MERT	98.56%	93.24%	94.65%	88.43%	96.57%	90.66%	90.21%	86.09%
MLDA	96.42%	92.13%	98.17%	95.86%	97.29%	93.73%	92.50%	89.70%
SSVM	98.03%	78.84%	84.58%	69.51%	90.81%	73.03%	69.65%	71.37%
SGNB	53.91%	50.60%	83.32%	86.58%	65.46%	61.61%	14.39%	46.47%
SRF	98.52%	90.12%	92.07%	82.81%	95.19%	86.07%	85.97%	82.39%
SERT	98.54%	91.86%	93.77%	86.08%	96.10%	88.74%	88.63%	84.42%
SLDA	98.30%	94.31%	98.43%	95.29%	98.36%	94.76%	96.25%	91.38%

E. Comparison with other commonly used methods

In order to further demonstrate the advantages of the TELRT algorithm proposed in this paper, we also considered the diagnostic performance of several traditional algorithms commonly used in fault diagnosis problems for PCB multiple faults. Besed on the measured scalar magnetic field data, the same data form as TELRT input data and the variety of different principles are considered to achieve different diagnosis processes, explicitly involving the algorithms as shown below:

1) Support Vector Machine (SVM): It uses the optimal hyperplane to separate different categories while maximizing the distance between the data on both sides of the boundary. For data, it maps the data to a high-dimensional space through a kernel method so that linearly inseparable data can be linearly separated, thereby achieving complex fault diagnosis tasks.
2) Gaussian Naive Bayes (GNB): It assumes that the fault features are conditionally independent and follow the

Gaussian distribution. It uses the Bayesian theorem to calculate the posterior probability that the data may belong to each fault type to implement the fault diagnosis method.

3) Random Forest (RF): It is an algorithm that trains multiple decision trees by randomly selecting data and features and uses voting to determine the fault type. Its randomness makes it more robust and less prone to overfitting when performing complex diagnostic problems.
4) Extremely Randomized Trees (ERT): It is an improved version of the RF algorithm. It not only randomly selects a subset of the dataset but also selects a random threshold when partitioning the features. This additional randomness gives the algorithm more vital generalization ability and training speed and can better adapt to complex diagnostic tasks of more data types.
5) Linear Discriminant Analysis (LDA): It is a linear model used for dimensionality reduction and classification. It assumes that the data follows a Gaussian distribution with the same covariance matrix and determines the fault type by finding the projection direction that maximizes the variance between faults and minimizes the variance within a class.

According to the basic principles of each algorithm, we evaluate the performance of these traditional algorithms on OP, CP, OR, CR, OF1, CF1, ACC, and mAP when they are combined with scalar magnetic field and scalar magnetic field source as input based on the same PCB state types and state combinations as TELRT in Table I. Here, the algorithms of SVM, GNB, RF, ERT, and LDA combined with magnetic field are named MSVM, MGNB, MRF, MERT, and MLDA, while the algorithms combined with magnetic field source are named SSVM, SGNB, SRF, SERT, and SLDA. Table III records the specific performance indicators of all traditional algorithm combinations.

From the indicators shown in Table III, some traditional methods can also perform relatively well in PCB multi-fault diagnosis. Specifically, by comparing the data in Table II and Table III, it can be found that the neural network algorithm with the self-attention mechanism proposed in this paper can effectively achieve higher and more balanced ACC (accuracy) and mAP (mean average precision) the two most critical fault diagnosis indicators. Table III shows that some traditional methods have high ACC but relatively low mAP when facing PCB fault diagnosis problems, and the two are not balanced. For example, the ACC of MERT, MLDA, and SLDA are all high and greater than 90%, but the mAP is significantly lower than ACC. mAP is lower than ACC, which means that when the algorithm encounters an imbalance in the amount of data of different fault types, the balance of indicators will be affected. This phenomenon is mainly because mAP more strictly evaluates the prediction quality of each fault, while ACC only calculates whether all faults are entirely correct without considering the impact of confidence and category imbalance. Therefore, even if the model does not perform well for some faults, as long as most faults are correct, ACC is still high. In order to verify the judgment, Table IV shows the ACC and mAP of the four-fault diagnosis algorithms with the highest ACC and mAP in Table III without the normal state shown in Table I (This process is the same as Section IV D. to verify the performance of TELRT when the normal state is not included).

TABLE IV
TRADITIONAL ALGORITHM PERFORMANCE

Algorithm	MERT	SERT	MLDA	SLDA
ACC	92.64%	91.29%	94.36%	97.06%
mAP	95.31%	94.02%	95.99%	97.14%

It can be seen that when the normal state is not included, the mAP of the traditional method is higher than the ACC, which shows that the model's performance on different categories is more balanced and performs well on each fault, not just on the overall fault. In terms of algorithm balance, all methods mentioned in Table II have shown good performance, which also shows that the training process of the neural network can effectively extract and analyze the deep information of the data. Although there are differences in the overall performance of different methods, the reliability and balance of the algorithm can be effectively guaranteed in the PCB multi-fault diagnosis problem.

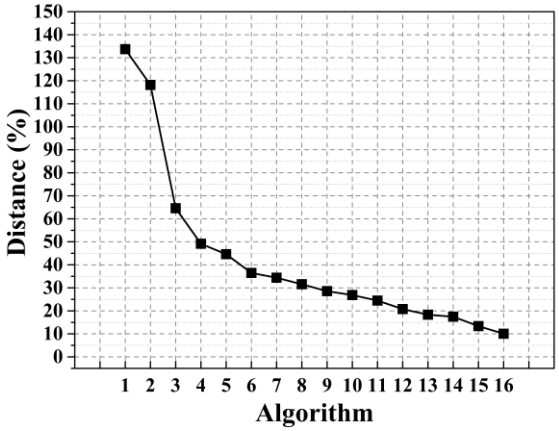

Fig. 11. Euclidean distance between algorithms metrics and 100%

In order to further visualize and compare the comprehensive performance of different algorithms in Table II and Table III, we regard OP, CP, OR, CR, OF1, CF1, ACC, and mAP as the performance coordinates of the fault diagnosis algorithm and the Euclidean distance from the coordinate to the 100% coordinate as a quantitative indicator to judge the comprehensive performance of different algorithms. The specific Euclidean distance calculation formula is as follows:

$$ED = \sqrt{\sum_{e=1}^{8}(p_e - p_o)^2} \tag{28}$$

where p_i and p_o are the actual values and the 100% values of OP, CP, OR, CR, OF1, CF1, ACC, and mAP. Fig. 11 shows the rearranging of all algorithms from left to right in ascending order, according to the values of the Euclidean distance. The numbers 1 to 16 on the horizontal axis in the figure correspond to algorithms SGNB, MGNB, SSVM, MSVM, MSFR, ESFR, SRF, MRF, SERT, MLSFR, MERT, ELSFR, ELRT, MLDA, SLDA, and TELRT. It can be seen from the Euclidean distance

curve that TELRT has obvious comprehensive advantages, and most algorithms in Table II perform better than those in Table III. Although the comprehensive performance of the LDA algorithm is slightly higher than that of other Table II algorithms except TELRT when all indicators are treated equally, as mentioned earlier, the balance of LDA in the two most critical indicators, ACC and mAP, is weak. In addition, we can find that fault diagnosis algorithms with more robust nonlinear capabilities are more suitable for extracting complex scalar magnetic field source features by combining the data in Figure 11, Table II, and Table III. The magnetic field source feature introduces the influence of the wave number term containing frequency, giving it more significant nonlinearity and richer radiation information. It is not difficult to find that the scalar magnetic field source feature can give the algorithm a higher performance ceiling, but its complexity can easily cause the simple algorithm structure to be too sensitive, resulting in performance degradation. The combination of the self-attention mechanism, fault-related auxiliary features, and neural networks proposed in this paper can effectively realize the analysis of the local and global relationship of complex features, make full use of the complex network structure to simulate the nonlinear relationship between complex features and faults, and make the algorithm have strong reasoning and nonlinear learning capabilities.

V. Conclusion

This article describes and verifies a non-contact PCB multi-fault diagnosis algorithm based on a scalar magnetic feature, fault relationship feature, and the Transformer architecture. We transformed the scalar field into the form of the scalar source and established the main feature that characterizes the behavior of the scalar source through the LBP algorithm. Meanwhile, we also use the topological relationship between fault types, establishing the auxiliary feature to fuse with the main features. Based on theoretical derivation, the article verifies the effectiveness and feasibility of the features and algorithms by simulating on/off faults, matching faults, performance degradation faults, and multi-type combination faults of the dual-phase amplification circuits. In the end, the calculation results of the proposed algorithm on actual test data show that the algorithm in this paper has excellent performance, achieving 98.55%, 94.89%, 98.55%, 95.11%, 98.55%, 95.32%, 96.01%, and 97.27% in multiple indicators such as OP, CP, OR, CR, OF1, CF1, ACC, and mAP, which results is higher than all existing traditional algorithms and neural network algorithms considered in this paper. In the future, based on the research content of this article, the research can be further attempted to achieve the PCB multi-fault diagnosis by adding multiphysics.

Appendix

No measurement method has an absolute advantage, but each has its advantages when dealing with different problems. In order to provide a more objective data selection reference and fully reveal the advantages of non-contact electromagnetic data as input in PCB fault diagnosis problems (without denying other data sources), we have compared in detail the traditional contact measurement, non-contact visual measurement, non-contact temperature measurement, and non-contact magnetic field measurement.

For contact measurement methods, contact probes connect different instruments to measure voltage, current, resistance, power, or S parameters to determine the PCB status, which is usually simple and intuitive, and the measured data is highly accurate. It is worth noting that contact measurement methods make it difficult to eliminate the influence of parasitic parameters in the measurement probe and the contact wear on the circuit. These situations may have a small impact on low-frequency PCBs, but for high-frequency PCBs, the *pF* level capacitance introduced by the probe and some circuit damages are sufficient to affect the circuit's distributed parameters and matching status. This situation will make determining PCB status highly dependent on the work experience of the inspection personnel. In addition, contact measurement relies heavily on probes or test points and must be manually measured one by one, making it challenging to cover all nodes of the circuit board. Especially for larger RF PCBs, it is even more challenging to ensure comprehensive measurement.

For non-contact methods, visual data can be obtained using cameras or microscopes, which usually have high resolution. Moreover, images, as a direct presentation of object morphology, are incredibly suitable for diagnosing wire breakage, short circuit, circuit damage, welding problems, and component loss. However, when there are obstructions and blind spots in the PCB, it can make it challenging to obtain compelling measurement data. In addition, visual data does not include the physical properties of PCBs, so it cannot handle faults that include the electrical characteristics of circuits.

As temperature and electromagnetic field data contain the physical characteristics of PCBs, they can effectively utilize physical laws to reflect some PCB electrical faults, which gives them more significant potential for development in solving complex PCB mechanism problems. The temperature data mainly uses Joule's law and heat conduction equation, as shown below, to describe the heat generation and heat transfer of PCB:

$$\begin{cases} Q = I_{RMS}^2 Rt \\ \frac{\partial T(\overrightarrow{r_1})}{\partial t} = \alpha \cdot \nabla^2 T(\overrightarrow{r_1}) + q(\overrightarrow{r_1}) \end{cases} \tag{29}$$

where Q is the heat, I_{RMS} is the effective current value, R is the impedance value, $T(\overrightarrow{r_1})$ is the temperature value, $\overrightarrow{r_1}$ is the temperature position, α is the thermal diffusion coefficient, and $q(\overrightarrow{r_1})$ is the heat source term. The temperature data generated by PCB depends to some extent on the accumulation and diffusion of heat over time, making it sensitive to detecting issues such as long-term high load and insufficient heat dissipation in PCB. However, due to the thermal diffusion effect, the temperature data is relatively smooth, and the resolution performance of local details of PCB is relatively weak. The used non-contact temperature measurement devices mostly use the Stefan Boltzmann Law, as shown below, to convert temperature data by measuring the surface thermal radiation P of objects:

$$P = \varepsilon\sigma T^4 = \varepsilon \cdot \sigma \cdot \left(\frac{Q}{m \cdot \theta} + T_0\right)^4 \tag{30}$$

where ε is the emissivity, σ is the Stefan Boltzmann law, T is the absolute temperature, m is the mass, θ is the specific heat capacity, T_0 is the initial temperature. It can be seen that thermal radiation is not directly related to frequency but is related to the effective value of current. This feature further indicates that temperature is more of a macroscopic measure and cannot directly reflect the state changes caused by various frequency components in the PCB. The characteristics of temperature data limit its ability to characterize PCB states with rich frequency features, such as RF PCBs. In addition, the PCB design concept of better heat dissipation and lower energy loss also limits the application of temperature data.

The electromagnetic field data is mainly described using the Maxwell equations composed of Ampère-Maxwell Law, Faraday's Law of Induction, Gauss's Law for Magnetism, and Gauss's Law for Electricity. The complete Maxwell equation system is shown below:

$$\begin{cases} \nabla \times \vec{H}(\vec{r}) = j\omega\varepsilon_0\vec{E}(\vec{r}) + \vec{J}(\vec{r_0}) \\ \nabla \times \vec{E}(\vec{r}) = -j\omega\mu_0\vec{H}(\vec{r}) \\ \nabla \cdot \vec{H}(\vec{r}) = 0 \\ \nabla \times \vec{E}(\vec{r}) = \frac{\rho(\vec{r_0})}{\varepsilon_0} \end{cases} \tag{31}$$

where $\vec{r}$ is the magnetic field coordinate, $\vec{r_0}$ is the current source coordinate, ε_0 is the dielectric constant, μ_0 is the magnetic permeability, $\omega = 2\pi f$, f is the frequency, $\vec{J}(\vec{r_0})$ is the current source, and $\rho(\vec{r_0})$ is the charge density. The Maxwell equations show the changes and generation in electric and magnetic fields. We can significantly find that as the frequency increases, the rate of change in electric and magnetic fields also increases, resulting in significant changes in the energy distribution, phase characteristics, and propagation features of electromagnetic waves. It is worth noting that the Maxwell equations exhibit the wave nature of electromagnetic waves, including the generation and transmission of energy from radiation sources, which show that signals can generate reflection, interference, and diffraction phenomena. Opposite, Eq. (29) shows that temperature does not have the wave-like behavior. It is a one-way accumulation of heat and a gradual flow from high-temperature to low-temperature areas, which is gradual and usually tends to stabilize unidirectionally. These physical laws indicate that the electromagnetic field tends towards dynamic equilibrium, while temperature tends towards static equilibrium. Most used non-contact electromagnetic measurement devices utilize the radiation characteristics of electromagnetic fields to receive radiated electric or magnetic fields. Here, in order to correspond to the radiation energy of temperature fields, we have listed the following formula for magnetic/electric dipole radiation sources:

$$P = \frac{m_0^2 \cdot \omega^4}{12 \cdot \pi \cdot \mu_0 \cdot c^3} = \frac{p_0^2 \cdot \omega^4}{12 \cdot \pi \cdot \mu_0 \cdot c^3} \tag{32}$$

where m_0 is the magnetic dipole, p_0 is the electric dipole, c is the speed of light. It can be seen that electromagnetic radiation is closely related to frequency and will rapidly increase with the increase of frequency. It further illustrates that electromagnetic fields can fully reflect the electromagnetic distribution characteristics in space and the state changes exhibited by different frequency components in PCBs. Electromagnetic measurement methods that include spatial and frequency characteristics can better grasp subtle changes in PCBs, which enhances their ability to characterize faults in complex high-frequency PCBs. However, more powerful feature analysis algorithms are required to analyze helpful information.

REFERENCES

[1] K. Dang et al., "Lateral GaN Schottky Barrier Diode for Wireless High-Power Transfer Application with High RF/DC Conversion Efficiency: From Circuit Construction and Device Technologies to System Demonstration," *IEEE Trans. Ind. Electron.*, vol. 67, no. 8, pp. 6597-6606, Aug. 2020.

[2] C. Liu et al., "A Sensor for 3-D Component Measurement of Synthetic Electric Field Vector in HVDC Transmission Lines Using Unidirectional Motion," *IEEE Trans. Instrum. Meas.*, vol. 72, pp. 1-10, Nov. 2023.

[3] C. Li et al. "A Review on Recent Progress of Portable Short-Range Non-contact Microwave Radar Systems," *IEEE Trans. Microwave Theory Tech.*, vol. 65, no. 5, pp. 1692-1706, May 2017.

[4] Z. Liu et al., "Open-Circuit Fault Diagnosis for MMC Based on Event-Triggered and Capacitor Current State Observation," *IEEE Trans. Circuits Syst. II Express Briefs*, vol. 69, no. 2, pp. 534-538, Feb. 2022.

[5] C. Liu et al., "A Calculation Method for Reconstructing Radiation State of PCB Using Known Magnetic Field Amplitude Information," *IEEE Trans. Instrum. Meas.*, vol. 73, pp. 1-13, Oct. 2024.

[6] N. Soveiko et al., "On the steady-state analysis of nonlinear circuits with frequency dependent parameters in wavelet domain," *IEEE Microw. Wirel. Compon. Lett.*, vol. 15, no. 5, pp. 384-386, May 2005.

[7] D. Tsai et al., "Machine Vision-Based Positioning and Inspection Using Expectation–Maximization Technique," *IEEE Trans. Instrum. Meas.*, vol. 66, no. 11, pp. 2858-2868, Nov. 2017.

[8] A. Stoynova et al., "Thermographic Approach for Reliability Estimation of PCB," *2018 41st International Spring Seminar on Electronics Technology (ISSE)*, Serbia, Aug. 2018, pp. 1-7.

[9] N. Berger et al., "Non-contact High Resolution Microwave Scanning Measurement Technology," *Electronics Letters*, vol. 39, no. 14, pp. 47-48, Jul. 2003.

[10] W. -C. Wang et al., "A Machine Vision Based Automatic Optical Inspection System for Measuring Drilling Quality of Printed Circuit Boards," *IEEE Access*, vol. 5, no., pp. 10817-10833, Nov. 2017.

[11] C. R. Wagh, "Detection of Faulty Region on Printed Circuit Board with IR Thermography," *Int. J. Sci. Eng. Res.*, vol. 4, no, 11, pp. 1-4, Nov. 2013.

[12] R. G. Wright, "Spectroscopic Electromagnetic Analysis Approach to Non-Contact Circuit Board Test and Diagnosis," *2015 IEEE AUTOTESTCON*, USA, Nov. 2015, pp. 173-180.

[13] L. Lei et al., "Multi-scale Convolution-Based Probabilistic Classification for Detecting Bare PCB Defects," *IEEE Trans. Instrum. Meas.*, vol. 72, pp. 1-8, Dec. 2023.

[14] J. Zhu et al., "Printed Circuit Board Defect Visual Detection Based on Wavelet Denoising," *IOP Conference Series: Materials Science and Engineering*, vol. 392, pp. 062055, 2018.

[15] S. Y. Huang et al., "A VQ-based Approach to Thermal Image Analysis for Printed Circuit Boards Diagnosis," *IEEE Trans. Instrum. Meas.*, vol. 54, no. 6, pp. 2381-2388, Dec. 2005.

[16] W. He et al., "Generative Adversarial Networks with Comprehensive Wavelet Feature for Fault Diagnosis of Analog Circuits," *IEEE Trans. Instrum. Meas.*, vol. 69, no. 9, pp. 6640-6650, Sept. 2020.

[17] M. -S. Kim et al., "Adaptive TX Leakage Canceler for the UHF RFID Reader Front End Using a Direct Leaky Coupling Method," *IEEE Trans. Ind. Electron.*, vol. 61, no. 4, pp. 2081-2087, Apr. 2014.

[18] S. Patra et al., "Self-Operating Flyback Converter for Boosting Ultra-Low Voltage of Thermoelectric Power Generator for IoT Applications," *IEEE Trans. Ind. Electron.*, vol. 69, no. 12, pp. 12957-12966, Dec. 2022.

[19] G. Shen et al., "Ultra-Low-Loss Millimeter-Wave LTCC Bandpass Filters Based on Flexible Design of Lumped and Distributed Circuits," *IEEE Trans. Circuits Syst. II Express Briefs*, vol. 68, no. 4, pp. 1123-1127, Apr. 2021.

[20] W. C. Chew et al., "Quantum Maxwell's Equations Made Simple: Employing Scalar and Vector Potential Formulation," *IEEE Antennas Propag. Mag.*, vol. 63, no. 1, pp. 14-26, Feb. 2021.

[21] X. Jin et al., "Investigation on the Electromagnetic Surface Waves for Single-Wire Power Transmission," *IEEE Trans. Ind. Electron.*, vol. 70, no. 3, pp. 2497-2507, Mar. 2023.

[22] R. G. Wright, "Circuit card test and diagnosis using electromagnetic emission analysis," *2012 IEEE AUTOTESTCON Proceedings,* Anaheim, Sep. 2012, pp. 324-329.

[23] H. Huang et al., "Electronic counterfeit detection based on the measurement of electromagnetic fingerprint," *Microelectron. Reliab*., Vol. 55, no. 9, pp. 2050-2054, Oct. 2015.

[24] Z. Yao et al., "Fault Diagnosis Using Magnetic Image of PCB," *Proceedings of 2012 UKACC International Conference on Control*, UK, Sep. 2012, pp. 702-707.

[25] H. F. Spence, "Printed Circuit Board Diagnosis Using Artificial Neural Networks and Circuit Magnetic Fields," *IEEE Aerosp. Electron. Syst. Mag.*, vol. 9, no. 2, pp. 20-24, Feb. 1994.

[26] K. Volkan et al., "Detection of Defects in Printed Circuit Boards with Machine Learning and Deep Learning Algorithms," *Avrupa. Bilim. Ve. Teknoloji. Dergisi.*, vol., no. 41, pp. 183-186, Nov. 2022.

[27] M. Amar et al., "Vibration Spectrum Imaging: A Novel Bearing Fault Classification Approach," *IEEE Trans. Ind. Electron.*, vol. 62, no. 1, pp. 494-502, Jan. 2015.

[28] K. M. M. Colwell, "Dualities, Helicity Amplitudes, and Little Conformal Symmetry," Cham, Switzerland: Springer International Publishing, 2017.

[29] S. QI et al., "Surface Defect Recognition of CSP Typical Slab Based on Improved ResNet," *2020 Chinese Automation Congress (CAC)*, China, Nov. 2020, pp. 6663-6667.

[30] EMSCAN, "EMxpert EHX User Manual," emcfastpass.com, 2024. [Online]. Available: https://www.emcfastpass.com/test-equipment/wp-content/uploads/2016/10/EMxpert_EHX_User_Manual_v5.0.6.1-10.15.pdf. Accessed on: May 6, 2024.

[31] S. Y. Sen et al., "Convolutional Neural Network Hyperparameter Tuning with Adam Optimizer for ECG Classification," *2020 Innovations in Intelligent Systems and Applications Conference (ASYU)*, Turkey, Oct. 2020, pp. 1-6.

[32] T. Chen et al., "Learning Semantic-Specific Graph Representation for Multi-Label Image Recognition," 2019 IEEE/CVF International Conference on Computer Vision (ICCV), Korea (South), Oct. 2019, pp. 522-531.

Chengxin Liu was born in Xianyang, Shaanxi Province, China 1996. He is pursuing a double Ph.D. in Beihang University and Politecnico di Torino, Beijing and Turin, China and Italy. He received the BS and MS degrees from Xi'an University of Posts & Telecommunications and Xidian University, Xi'an, China, in 2018 and 2021, respectively.

His current research interests include computational electromagnetics and the detection method of PCB, as well as the development of advanced electromagnetic field detection equipment.

Haiwen Yuan was born in Baoji, Shaanxi Province, China, in 1968. He received a BS, MS, and Ph.D. in electrical engineering from Xi'an Jiaotong University, China, in 1990, 1993 and 1996, respectively.

He is currently a professor and a doctoral supervisor at Beihang University, Beijing, China. He is the author of more than 140 articles. He holds more than 40 patents in China. His research interests include detection technology and automation devices, power electronics, particularly power supply, and embedded systems.

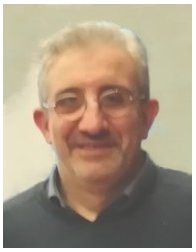

Michele Ferlauto received his MS (1993) and Ph.D. in Aerospace Engineering (1997) at Polytechnical University of Turin and Milan, respectively.

He is currently a professor and doctoral supervisor with Politechnical University of Turin (Politecnico di Torino), Italy. He has proposed innovative contributions on the solution of inverse problems in different fields and on its coupling with adjoint optimization techniques. His current research interests include optimal design and instability detection in aerospace systems, active flow control.

Jianxun Lv was born in Xi'an, Shaanxi Province, China, in 1984. He received his BS and Ph.D. in control science and engineering from Beihang University, China, in 2006 and 2014, respectively.

He is currently working as an associate professor, Beihang University, China. He is the author of more than 30 articles. His current research interests include measurement technology, sensor technology, and electromagnetic environment detection.

Yingyi Liu was born in Shandong Province, China, in 1980. She received a Ph.D in electrical engineering from Xi'an Jiaotong University, China, in 2009. Since 2009, she has been with the School of Automation Science and Electrical Engineering at Beihang University. Her research interests focus on the electromagnetic environment of ultrahigh-voltage DC transmission lines.

Hai Xu was born in Wuhu, Anhui Province, China 1981. He received the BS and MS degrees from Hefei University of Technology and Nanjing University of Aeronautics and Astronautics, respectively.

He currently works with the Wuhu Machinery Factory, Wuhu, China, focusing on fault diagnosis.